Journal of Alloys and Compounds 870 (2021) 159376

Contents lists available at ScienceDirect

Journal of Alloys and Compounds

journal homepage: www.elsevier.com/locate/jalcom

Plasma-implanted Ti-doped hematite photoanodes with enhanced photoelectrochemical water oxidation performance

Yong Peng[a,c,d], Qingdong Ruan[b,c], Chun Ho Lam[a], Fanxu Meng[e], Chung-Yu Guan[f], Shella Permatasari Santoso[g,h], Xingli Zou[i], Edward T. Yu[j], Paul K. Chu[b,c], Hsien-Yi Hsu[a,c,d,*]

[a] School of Energy and Environment, City University of Hong Kong, Tat Chee Avenue, Kowloon Tong, Hong Kong, China
[b] Department of Physics, City University of Hong Kong, Tat Chee Avenue, Kowloon, Hong Kong, China
[c] Department of Materials Science and Engineering, City University of Hong Kong, Tat Chee Avenue, Kowloon, Hong Kong, China
[d] Shenzhen Research Institute of City University of Hong Kong, Shenzhen 518057, China
[e] Institute of Microscale Optoelectronics, International Collaborative Laboratory of 2D Materials for Optoelectronics Science and Technology, College of Physics and Optoelectronic Engineering, Shenzhen University, Shenzhen 518060, China
[f] Department of Environmental Engineering, National Ilan University, Yilan 260, Taiwan, ROC
[g] Chemical Engineering Department, Widya Mandala Surabaya Catholic University, East Java, Indonesia
[h] Chemical Engineering Department, National Taiwan University of Science and Technology, Taipei, Taiwan, ROC
[i] State Key Laboratory of Advanced Special Steel, School of Materials Science and Engineering, Shanghai University, Shanghai 200444, China
[j] Microelectronics Research Center, Department of Electrical and Computer Engineering, the University of Texas at Austin, Austin 78758, Texas

ARTICLE INFO

Article history:
Received 4 December 2020
Received in revised form 6 February 2021
Accepted 1 March 2021
Available online 6 March 2021

Keywords:
Hematite
Photoelectrochemistry
Surface engineering
Plasma ion implantation

ABSTRACT

Hematite (α-Fe_2O_3) is recognized as a promising photoelectrode material for photoelectrochemical (PEC) water splitting, as a result of its abundance, non-toxicity, suitable bandgap, and photochemical stability. Nevertheless, the undesirable physical and photophysical behaviors, such as poor conductivity, short diffusion length, and rapid charge-carrier recombination, seriously restrict PEC water splitting efficiency of hematite semiconductors. Herein, we fabricate nanoporous titanium (Ti)-doped α-Fe_2O_3 thin films by a facile hydrothermal reaction, subsequently utilizing energetic plasma ion implantation with a post-annealing process to significantly enhance the photoelectrochemical water oxidation performance of hematite. On the basis of materials characterization and electrochemical analysis, the optimized Ti-doped Fe_2O_3, i.e., Ti-4-Fe_2O_3, exhibits improved photocurrents of 0.55 and 1.07 mA cm^{-2} at 1.23 and 1.5 V versus RHE respectively under illumination of 100 mW/cm^2 with AM 1.5 G spectrum, showing approximately 1.6-fold increases compared to pristine Fe_2O_3. We attribute this increase to improved charge carrier transport induced by Ti doping that reduces the recombination of light-driven charge carriers. The work utilizing plasma-assisted doping technique provides new insights into the surface engineering of photo-responsive semiconductors for the development of emerging hydrogen technologies.

1. Introduction

Solar energy has been recognized as one of the most promising and cost-competitive renewable energy alternatives for the replacement of conventional fossil fuels. Photoelectrochemical (PEC) water splitting is an attractive approach to convert renewable light energy into chemical energy for practical applications, owing to the facile storage and transportation of hydrogen. In the field of solar water splitting, we still face the challenge related to the cost-effective fabrication of robust photo-responsive materials with high performance in an economic way. Among the most favorable semiconductors, e.g. $BiVO_4$, WO_3 and Fe_2O_3 for PEC water oxidation, there is no doubt that hematite (α-Fe_2O_3) is a promising photoanode candidate as a result of its chemical stability, environmental friendliness, earth abundance as well as a suitable bandgap (~2.1 eV) that achieves a theoretical solar-to-hydrogen efficiency of ~16% [1]. Despite these advantages, hematite suffers from ultrafast electron-hole recombination (~10 ps), short hole diffusion length (2–4 nm) and slow oxygen evolution reaction (OER) activity [2]. Various strategies have been developed to overcome these obstacles.

Elemental doping is a highly practical approach to improve the PEC performance. Among various elements, e.g. Ti [3], Sn [4], and P

* Corresponding author at: School of Energy and Environment, City University of Hong Kong, Tat Chee Avenue, Kowloon Tong, Hong Kong, China.
E-mail address: sam.hyhsu@cityu.edu.hk (H.-Y. Hsu).

https://doi.org/10.1016/j.jallcom.2021.159376
0925-8388/

[5], titanium doping of hematite photoanodes is a potential strategy. For instance, Franking et al. demonstrated that the addition of Ti precursor solutions on hematite films followed by annealing in atmosphere could promote Ti diffusion into hematite, resulting in the enhancement of its PEC response [6]. Ion implantation is an efficient technique for surface modification of conventional materials, such as alloys and polymers, to improve their mechanical properties (e.g. anti-corrosion, anti-wear and strength) and chemical properties (e.g. destruction and formation of chemical bonds) [7]. In recent years, the ion implantation technique has been introduced to modify and develop photoelectrodes. For example, Shen's group has reported that V [8], Cu [9] and W [10] ions could be implanted into ZnO lattices. The enhanced PEC performance of the ion implanted ZnO could be attributed to both improved visible light absorption and increased charge carrier density.

Controllable amounts of elemental doping and modification of surface morphology can both be realized by ion implantation. Herein, we fabricate efficient photoresponsive materials by utilizing this technique for improving the performance of PEC water splitting for hematite. After different doses of titanium implantation and subsequent post-annealing treatments, pristine and titanium plasma implantation treated hematite, i.e., Fe_2O_3, Ti-1-Fe_2O_3, Ti-2-Fe_2O_3, Ti-4-Fe_2O_3 and Ti-8-Fe_2O_3, were synthesized. The surface morphology of titanium plasma implantation treated hematite is moderately changed to the nanoporous structure. We observe well-distributed Ti doping on the surface, resulting in lower photoluminescence (PL) intensity as a result of reduced charge carrier recombination. The optimized Ti-implanted hematite, Ti-4-Fe_2O_3, exhibits the lowest charge transfer resistance and highest charge carrier density, resulting in a highest photocurrent density with a better stability compared to pristine hematite. To the best of our knowledge, this is the first report of hematite treated by using Ti plasma implantation for the enhancement of PEC water oxidation.

2. Experimental

2.1. Reagents and materials

Anhydrous $FeCl_3$ (99%, Alfa Aesar) and $NaNO_3$ (99.9%, DUKSAN) were used as received without further purification. Fluorine-doped tin oxide (FTO) coated glass (6–9 Ω/sq) was sliced to 1.5 × 3.0 cm pieces which were subsequently sonicated in deionized water, acetone and ethanol each for 20 min and then dried with compressed air before use. Ti rods (99.9999%, Shenzhen Morgan Sputtering Targets & Technology Co., China) were used as an ion beam source for implantation. All solutions were prepared using ultrapure water generated by Milli-Q water purification system.

2.2. Preparation of pristine α-Fe_2O_3 and titanium ion implanted α-Fe_2O_3

Hematite films were fabricated on fluorine-doped tin oxide (FTO) coated glass according to previous studies [11]. Typically, 2.433 g of $FeCl_3$ (0.15 M) and 8.50 g of $NaNO_3$ (1 M) were dissolved in ultrapure water and the volume was adjusted to 100 mL using a 100-mL volumetric flask. The pH of the solution was about 1.5 without the adjustment. After that, 20 mL of the precursor solution was added into each 30 mL Teflon liner containing a piece of FTO glass with FTO side facing down. The hydrothermal reactors were heated at 95 °C for 4 h in an oven. Consequently, akaganeite (β-FeOOH) coated on FTO glass could be obtained and was rinsed with ultrapure water several times. Next, the β-FeOOH was calcined at 550 °C for 2 h (ramp rate 2.5 °C min^{-1}) and then at 800 °C for 10 min (ramp rate 5 °C min^{-1}) under air atmosphere to obtain α-Fe_2O_3 in a tube furnace.

For titanium ion implantation treatment, the obtained β-FeOOH films were firstly treated with titanium ion beam generated from a metal vapor vacuum arc source by a broad-beam high energy ion implanter (Model HEMII-80, Plasma Technology Ltd.). Titanium ions were implanted with doses of 0 (a control sample), 1×10^{16}, 2×10^{16}, 4×10^{16} and 8×10^{16} atoms per centimeter square of the film at a voltage of 35 kV. The obtained materials were named as FeOOH, Ti-1-FeOOH, Ti-2-FeOOH, Ti-4-FeOOH and Ti-8-FeOOH, respectively. Afterwards, the titanium ion implanted β-FeOOH films were annealed under the same condition (550 °C for 2 h and then 800 °C for 10 min) to get titanium ion implanted α-Fe_2O_3. The as-prepared films were labeled as Fe_2O_3, Ti-1-Fe_2O_3, Ti-2-Fe_2O_3, Ti-4-Fe_2O_3 and Ti-8-Fe_2O_3, respectively.

2.3. Film characterization

The surface morphology of titanium ion implanted β-FeOOH and α-Fe_2O_3 were imaged by a ZEISS EVO MA10 SEM at a voltage of 15 kV. XRD patterns were collected using a PANalytical X′Pert^3 X-ray diffractometer between 10 and 70 degree with a tension of 40 kV and a current of 40 mA under Cu-Kα radiation (1.54 Å). Raman spectra were taken using a HORIBA HR800 Raman microscope with a 514-nm laser. XPS analysis was carried out using a Thermo Fisher ESCALAB 250Xi X-ray photoelectron spectrometer, and the binding energy was calibrated by the C 1s peak at 284.6 eV. Transmission electron microscope (TEM; JEOL JEM-2100 F) equipped with energy-dispersive spectrometer (EDS) was used to explore the elemental distributions and morphological changes. UV–visible absorption spectra were measured using a Shimadzu UV-3600 spectrophotometer equipped with an integrating sphere in the range from 800 to 300 nm. Photoluminescence (PL) spectra were collected with a 500-nm long-pass filter under an excitation wavelength of 450 nm by a Shimadzu RF-5301 PC spectrometer.

2.4. Electrochemical measurements

All the electrochemical tests were carried out with a electrochemical workstation (CHI 760E, Shanghai Chenhua Instruments Co., China) using a three-electrode system in which pristine or titanium ion implanted Fe_2O_3 film were used as a working electrode, Pt wire as counter electrode, and Ag/AgCl (in 3 M KCl) connected to electrolyte (1 M NaOH, pH 13.6) by a salt bridge (3 M KCl) as reference electrode. The electrolyte was purged with nitrogen for 10 min before all the following tests to prevent oxygen reduction reaction at the counter electrode. A working area of 0.283 cm^2 of the photoanodes was irradiated under 1-sun (100 mW/cm^2, AM 1.5 G) illumination, which used a 300-W xenon lamp with an AM 1.5 filter as light source for linear sweep voltammetry (LSV), electrochemical impedance spectroscopy (EIS), Mott-Schottky (MS) and amperometric i-t (I-t) measurements.

LSV measurements were conducted to evaluate the PEC water oxidation performance of the as-prepared titanium implanted α-Fe_2O_3. The potential was scanned from −0.6 to 0.6 V versus Ag/AgCl at a scan rate of 10 mV s^{-1}. The potential versus Ag/AgCl was converted to the potential versus reversible hydrogen electrode (RHE) according to the following equation:

$$E_{RHE} = E^{\ominus}_{Ag/AgCl} + E_{Ag/AgCl} + 0.059 \times pH$$

where E_{RHE} is the converted potential versus RHE, $E^{\ominus}_{Ag/AgCl}$ is the standard electrode potential of Ag/AgCl electrode against standard hydrogen electrode and equal to 0.210 V at 25 °C, and $E_{Ag/AgCl}$ is the experimentally measured potential versus Ag/AgCl electrode. For EIS tests, an initial potential was set at 0.22 V versus Ag/AgCl (equal to 1.23 V versus RHE) with the frequencies ranging from 10^5 to 0.5 Hz and an amplitude voltage of 10 mV under illumination. The collected EIS data were fitted using ZView software (Scribner and Associates Inc., USA). MS plots were collected at a frequency of 1 kHz from −0.6 to 0.4 V versus Ag/AgCl at an amplitude of 5 mV under dark

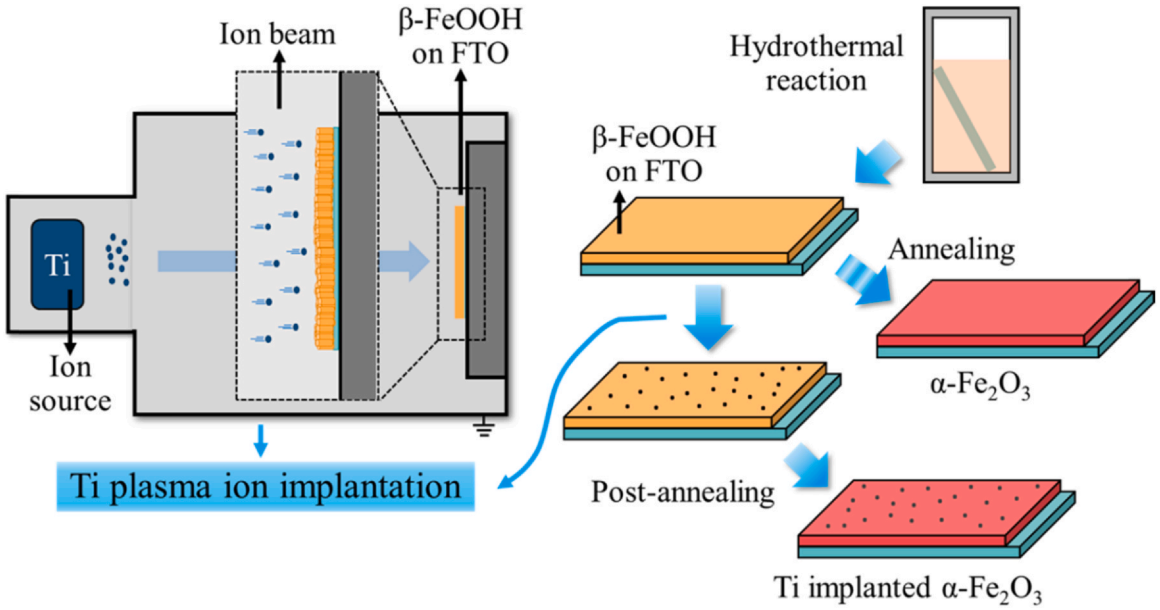

Scheme 1. Fabrication process of titanium ion implanted α-Fe_2O_3.

condition. Charge carrier densities can be estimated according to the following equation:

$$N_d = \frac{2}{\varepsilon\varepsilon_0 A^2 e} \times \left[\frac{d\left(\frac{1}{c^2}\right)}{dV}\right]^{-1}$$

where N_d is donor density (in m^{-3}), ε is relative permittivity ($\varepsilon = 80$ for hematite [12]), ε_o is vacuum permittivity ($\varepsilon_o = 8.85 \times 10^{-12}$ F m^{-1}), A is the surface area ($A = 2.83 \times 10^{-5}$ m^2 in this study), e is electronic charge ($e = 1.602 \times 10^{-19}$ C), c is interfacial capacitance (in F), and V is the applied voltage (in V). Amperometric i-t measurements were used to assess the stability of titanium ion implanted α-Fe_2O_3. During the I-t tests, the bias potential was set at 0.22 V versus Ag/AgCl (equal to 1.23 V versus RHE) and the measurements lasted for 5 h under illumination. A steady nitrogen flow was supplied into the cell to prevent oxygen from entering the electrolyte.

3. Results and discussion

The fabrication process of titanium plasma implanted hematite photoanodes is depicted in Scheme 1. For the preparation of titanium implanted α-Fe_2O_3, β-FeOOH films were first grown on FTO glass by using a conventional hydrothermal reaction. Afterwards, the β-FeOOH films were treated with different doses of titanium ions, subsequently converting to α-Fe_2O_3 by a post-annealing process under atmospheric conditions. Pristine hematite as a controlled photoanode was also synthesized in the absence of ion implantation treatments.

As shown in the photographs of Supplementary Fig. S1, the color of β-FeOOH films changed from yellow to dark brown in a dose-dependent manner after titanium ion implantation treatment. The uniform color also implies well-distributed Ti ions in the β-FeOOH film. All the treated β-FeOOH films turned to red after the post-annealing process at 550 °C for 2 h and subsequently at 800 °C for 10 min in order to recover the damage of lattice structure caused by ion implantation. As depicted in Fig. S2a–e, we observed that ion beam treatment could cause dose-dependent agglomeration of β-FeOOH nanorods and the formation of porous structures in the process. After calcination (Fig. 1a–e), the SEM images of titanium ion implanted α-Fe_2O_3 reveal that the aggregation of nanostructures give rise to large porous structure. The lateral feature size of nanoporous structures increases from 130 ± 20 nm in untreated Fe_2O_3 to 170 ± 20 nm in Ti-8-Fe_2O_3, depending on the amounts of implanted ions. Notably, the featured sizes have a significant influence on the functional properties of nanomaterials. With the report of Brillet et al. [13], hematite nanorods have been regulated to obtain a desired featured size of approximately 30–40 nm using a solution-based encapsulation strategy. They also indicated that smaller nanostructures are beneficial to electron-hole transfer at semiconductor/liquid interfaces under a high bias potential, in spite of the fact that small nanostructures have negative impacts on the onset potential. Because morphological change of titanium ion implanted α-Fe_2O_3 is not evident, we expect the PEC performance of hematite through morphology engineering would be modestly affected by ion implantation process.

The XRD patterns of the materials, shown in Fig. 2a, indicate the presence of β-FeOOH before the post-annealing process. Two peaks at 11.8 and 35.2 degree are attributed to the diffraction of (110) and (211) facets of akaganeite (JCPDS No. 34–1266), respectively. High intensity of the diffraction peak at 35.2 degree implies that the growth of these nanorods is along the [211] direction [11]. After titanium ion implantation, all diffraction peaks of β-FeOOH sharply decreased (Magnified in Fig. S3a–b), suggesting that Ti atoms have been implanted into the lattice structure of β-FeOOH, which causes disorder in the crystal structure. After calcination at high temperature, the XRD patterns of as-prepared materials (Fig. 2b) reveal the generation of α-Fe_2O_3 (JCPDS No. 33-0664). The peaks at 35.6 degree are ascribed to the diffraction of (211) facet [11]. Remarkably, although these peaks appeared in titanium ion implanted α-Fe_2O_3 after post-annealing, their intensities decreased compared to that of pristine α-Fe_2O_3 (Fig. 2c). Additionally, the XRD results do not exhibit the existence of TiO_2 or ilmenite in both β-FeOOH and α-Fe_2O_3.

Raman spectra of titanium ion implanted α-Fe_2O_3 (Fig. 3) have been characterized to further explore the change in crystal structure of titanium ion implanted α-Fe_2O_3. The intrinsic Raman peaks at 224 ($A_{1g}(1)$), 243 ($E_g(1)$), 292 ($E_g(1)$), 298 ($E_g(1)$), 410 ($E_g(1)$), 497 ($A_{1g}(2)$) and 610 ($E_g(1)$) cm^{-1} can be clearly detected from both pristine α-Fe_2O_3 and titanium ion implanted α-Fe_2O_3 [14]. Furthermore, the increased intensity of the peak at 660 cm^{-1} is attributed to the disorder-sensitive mode (E_u) of α-Fe_2O_3. This mode is theoretically not Raman-active in the Raman responses of hematite, while it is

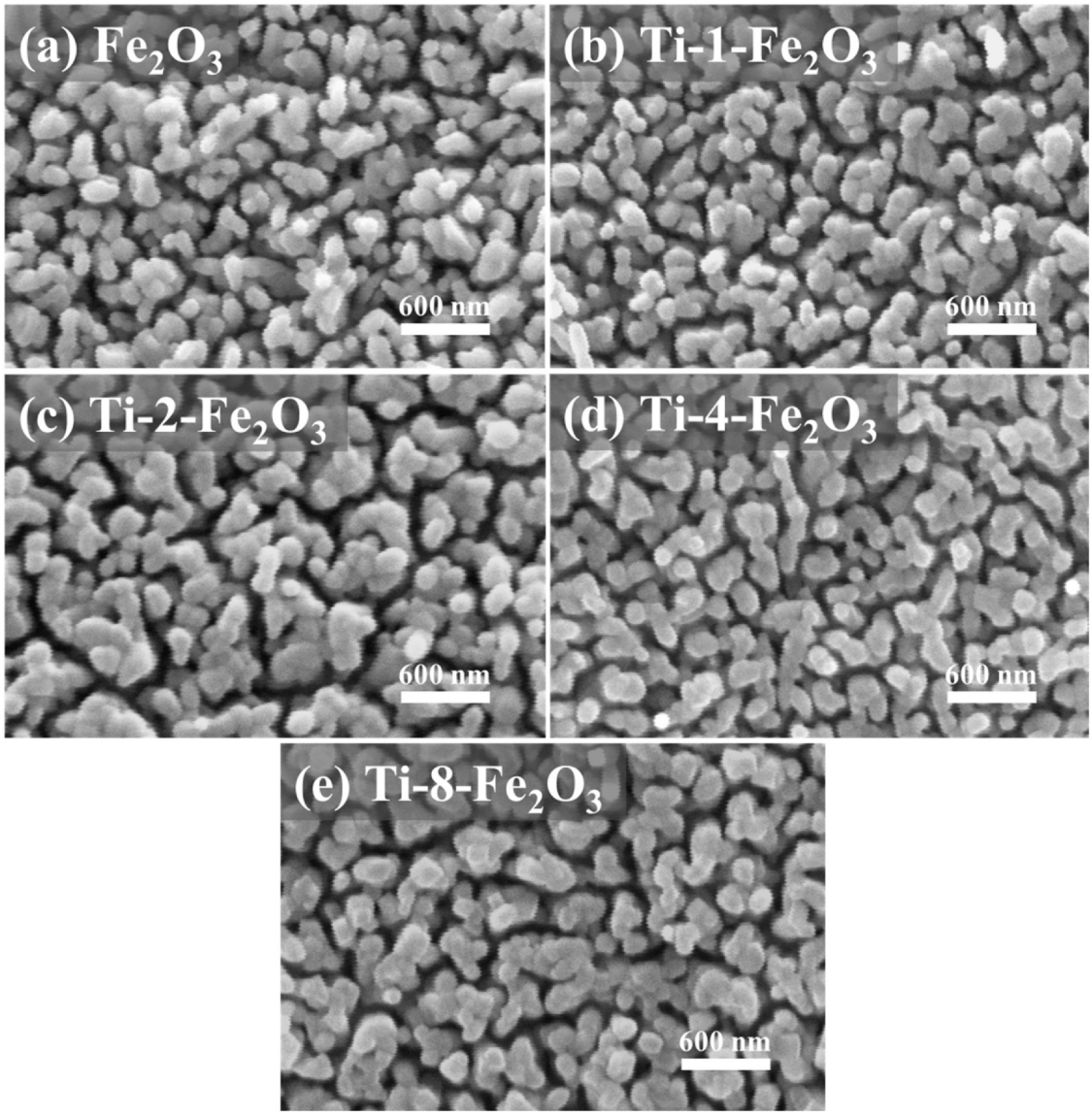

Fig. 1. SEM images of titanium ion implanted α-Fe_2O_3 at different doses: (a) Fe_2O_3, (b) Ti-1-Fe_2O_3, (c) Ti-2-Fe_2O_3, (d) Ti-4-Fe_2O_3 and (e) Ti-8-Fe_2O_3.

recognized as a E_u(LO) mode in the infrared measurements [14]. Despite that, imperfect surface symmetry and stress-induced defects (e.g., impure atoms in lattices) can activate strong responses at 660 cm^{-1}. Our Raman results are similar to that of Si-doped hematite, implying the incorporation of Ti atoms into the lattice of α-Fe_2O_3 [15]. In addition, we further observed a maximum intensity ratio of the peak at 660 cm^{-1} to the peak at 610 cm^{-1} in Ti-4-Fe_2O_3 (Table S1), which suggests a high degree of asymmetry in the bulk structure as well as considerable amounts of Ti doping in α-Fe_2O_3.

The full survey and high-resolution XPS spectra including O 1s, Fe 2p and Ti 2p of the Ti-4-Fe_2O_3 specimen were characterized (Fig. 4). In the survey spectrum (Fig. 4a), in addition to Fe and O, the elements including Ti, Sn, and C can also be detected. The detectable amount of Sn is possibly attributed to the diffusion of Sn from the FTO glass at high temperature [16]. The existing Ti atoms are arising from the dopants generated by titanium plasma implantation. The C 1s signal as a binding energy reference can be detected due to adventitious carbon contamination during air exposure. The Fe 2p high-resolution spectrum (Fig. 4b) shows two split spin-orbit components, Fe $2p_{1/2}$ and Fe $2p_{3/2}$, located at 724.3 and 710.7 eV, respectively, which are quite consistent with their reported binding energies in α-Fe_2O_3 [17]. Besides, the binding energy difference between the two components is 13.5 eV, clearly verifying the formation of Fe_2O_3 [18]. Additionally, surface peaks for Fe $2p_{1/2}$ and Fe $2p_{3/2}$ with high binding energies of 728.1 and 714.5 eV have been fitted. These surface peaks could be induced by disordered atomic arrangement at the surface of materials, which probably gives rise to low electron density surrounding the Fe(III) atoms, thus requiring high energy to eventually produce photoelectrons [19]. The oxidation state (i.e., Fe^{3+}) of the Fe has been confirmed by the satellite peaks of Fe $2p_{1/2}$ and Fe $2p_{3/2}$ at 732.7 and 718.2 eV, respectively [20]. The O 1s spectral region in Fig. 4c can be fitted with two peaks located at 530.0 and 531.4 eV, which can be assigned to lattice oxygen (Fe–O) and surface hydroxyl (O–H), respectively [21]. Importantly, the Ti 2p high-resolution spectrum (Fig. 4d) displays two components, Ti $2p_{1/2}$ and Ti $2p_{3/2}$, with binding energies of 464.0 and 458.3 eV, respectively, indicating Ti(IV) atoms surrounded by oxygen atoms [22]. The difference of binding energies between two split spin-orbit components is 5.7 eV, re-confirming the oxidation state (i.e., Ti^{4+}) of the implanted titanium atoms [23]. The two shake-up peaks at 465.0 and 459.4 eV presumably result from reduced kinetic energy of photoelectrons [24]. XPS depth profiling was also performed to analyze elemental distribution in the implantation direction. The profile of Ti-4-FeOOH reveals that titanium atoms can

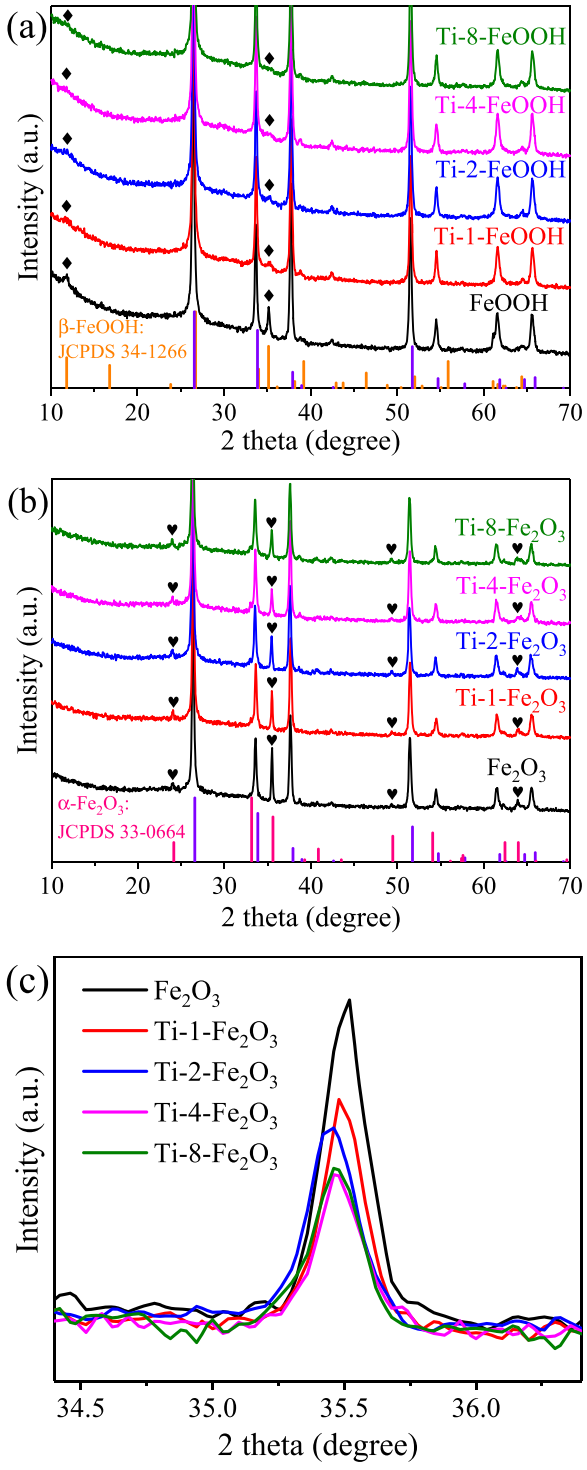

Fig. 2. XRD patterns of titanium ion implanted materials at different doses. (a) ion implanted β-FeOOH, (b) ion implanted α-Fe_2O_3 after post-annealing, and (c) magnified view of (211) peaks for ion implanted α-Fe_2O_3.

be implanted into β-FeOOH film at a depth of at least 180 nm (Fig S4). After the post-annealing process under atmospheric conditions for the formation of Ti-4-Fe_2O_3, more oxygen atoms were introduced into the film which can be observed by the increased oxygen percentage (Fig. 4e). The Ti/Fe atomic ratio of ~ 0.15 is also indicates a well-distributed Ti doping in the depth direction (Fig. 4f). The atomic percentage of iron at the surface is low probably because of carbon contamination.

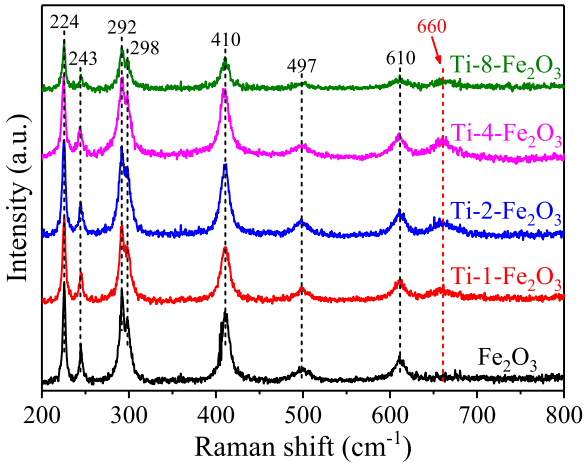

Fig. 3. Raman spectra of titanium ion implanted α-Fe_2O_3 at different doses.

The incorporation of Ti atoms into plasma ion implanted β-FeOOH and α-Fe_2O_3 was further investigated by TEM and corresponding mapping techniques. As shown in Fig. 5a, the TEM results indicate that Ti-4-FeOOH has a nanorod structure with a diameter of around 80 nm (solid blue line). Additionally, EDS mapping was used to evaluate the influence of direct Ti bombarding on the spatial distribution of Fe, O and Ti elements. The signal of element Ti has been observed in an extended area of Ti-4-FeOOH, indicating that the energetic ion implantation technique enables the penetration of Ti atoms into the deep area of the material, which is consistent with the results of XPS depth profile. Besides, the mapping images also present evenly distributed Fe and O atoms in the nanostructured Ti-4-FeOOH. After annealing the material in synthetic air, the obtained Ti-4-Fe_2O_3 displays an aggregated bulk-like nanostructure (Fig. 5b). The elemental mapping of Ti-4-Fe_2O_3 clearly reveals the presence of Ti with Fe and O, where a well-distributed Ti element has been observed in a width of ca. 400 nm.

The optical absorption properties of pristine and titanium ion implanted Fe_2O_3 films were evaluated by UV–visible absorption spectroscopy (Fig. 6a). The spectra with an absorption onset at 600 nm exhibit a typical characteristic of hematite films. The Tauc plot $(\alpha h\nu)^{1/r} \sim h\nu$, where α represents absorption coefficient of the material; h is Planck constant; ν is frequency of photon; and r is the nature of the transition and equal to 2 for indirect allowed transitions, can be used to estimate the bandgap of semiconductors [1]. As shown in the inset table of Fig. 6b, Tauc plots derived from the absorption spectra of as-prepared α-Fe_2O_3 (Fig. 6b) yield bandgaps that are largely independent of titanium ion implantation treatment, revealing an indirect bandgap of 2.05–2.06 eV for all the α-Fe_2O_3, which is in accordance with previous literature [3]. The Ti-dopped semiconductor still retained more than 95% of the initial absorption after 35 days of exposure. Photoluminescence (PL) spectra of as-prepared pristine and titanium ion implanted α-Fe_2O_3 films were carried out under an excitation wavelength of 450 nm to monitor the recombination of charge carriers in the bulk and at the surface (Fig. S5). The PL emission recorded from 520 to 750 nm exhibits a broad emission peak at around 620 nm for both pristine α-Fe_2O_3 and titanium ion implanted α-Fe_2O_3, which is in line with previous report [25]. The PL emission, which is mainly attributed to the recombination of photogenerated electrons and holes, could serve as an indicator to indirectly evaluate the efficiency of charge carrier transport [26]. As shown in Fig. S5, Ti-4-Fe_2O_3 shows the lowest PL intensity, suggesting suppressed recombination of photogenerated charge carriers due to improved diffusion rate [27], potentially leading to the enhancement of photoactivity. Further investigation on the reduced charge recombination centers in Ti-incorporated

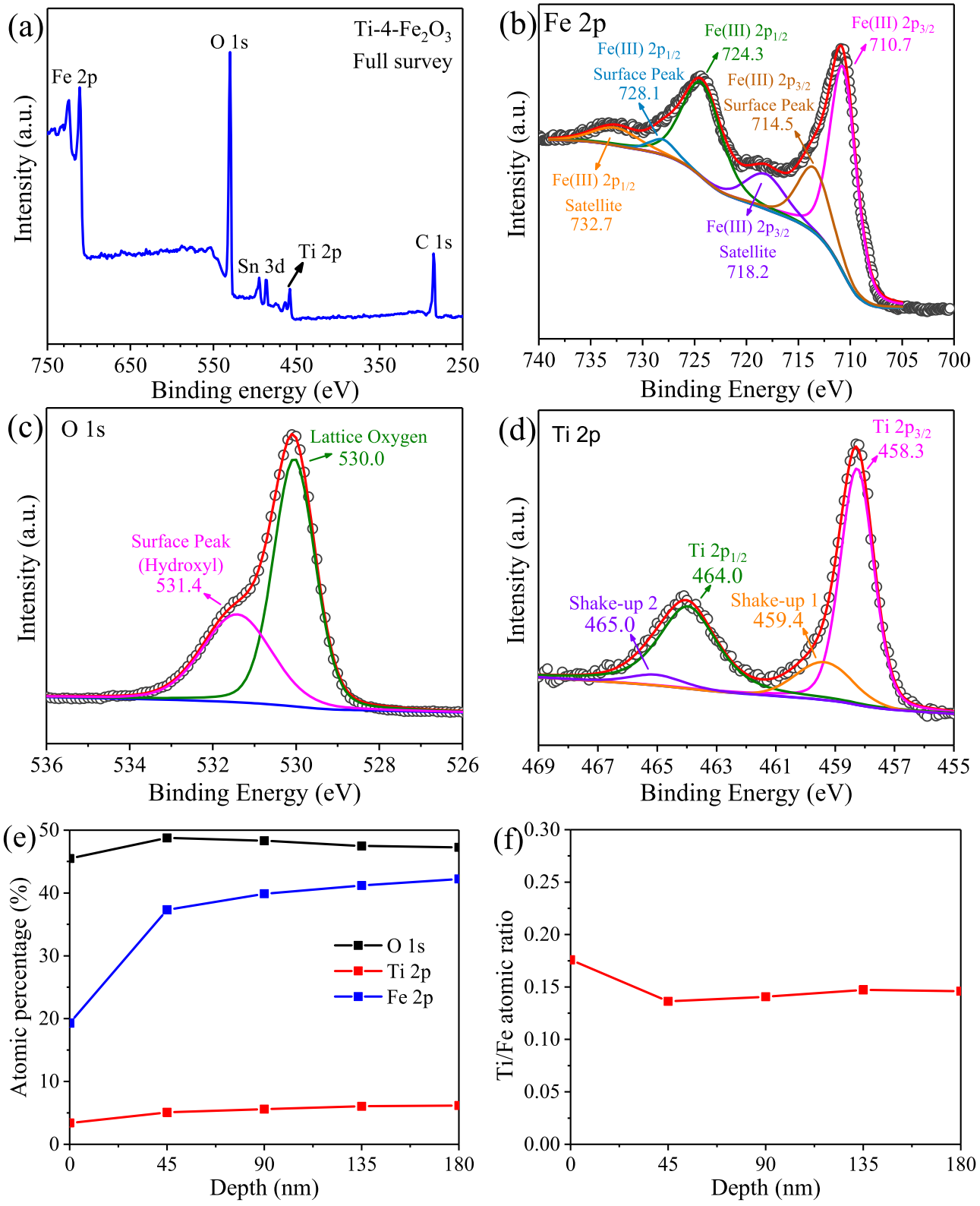

Fig. 4. XPS spectra collected from Ti-4-Fe_2O_3: (a) full survey, (b) Fe 2p, (c) O 1 s, (d) Ti 2p, (e) depth profile and (f) Ti/Fe atomic ratio.

hematite is of importance to understand the roles of doping in photoelectrodes.

The charge transfer characteristic of these titanium ion implanted α-Fe_2O_3 photoanodes was explored by electrochemical impedance spectroscopy (EIS). As shown in the Nyquist diagram (Fig. 7a), the EIS spectra were fitted based on the equivalent circuit in the inset of Fig. 7a using Zview software [28]. The 1-RC equivalent circuit model contains a RC circuit, including a charge transfer resistance at electrode||electrolyte interface (R_{ct}), a parallel double-layer capacitance (CPE), as well as a series resistance (R_s). As listed in fitting results of Table S2, hematite implanted with different doses of titanium show lower charge transfer resistance compared to that of

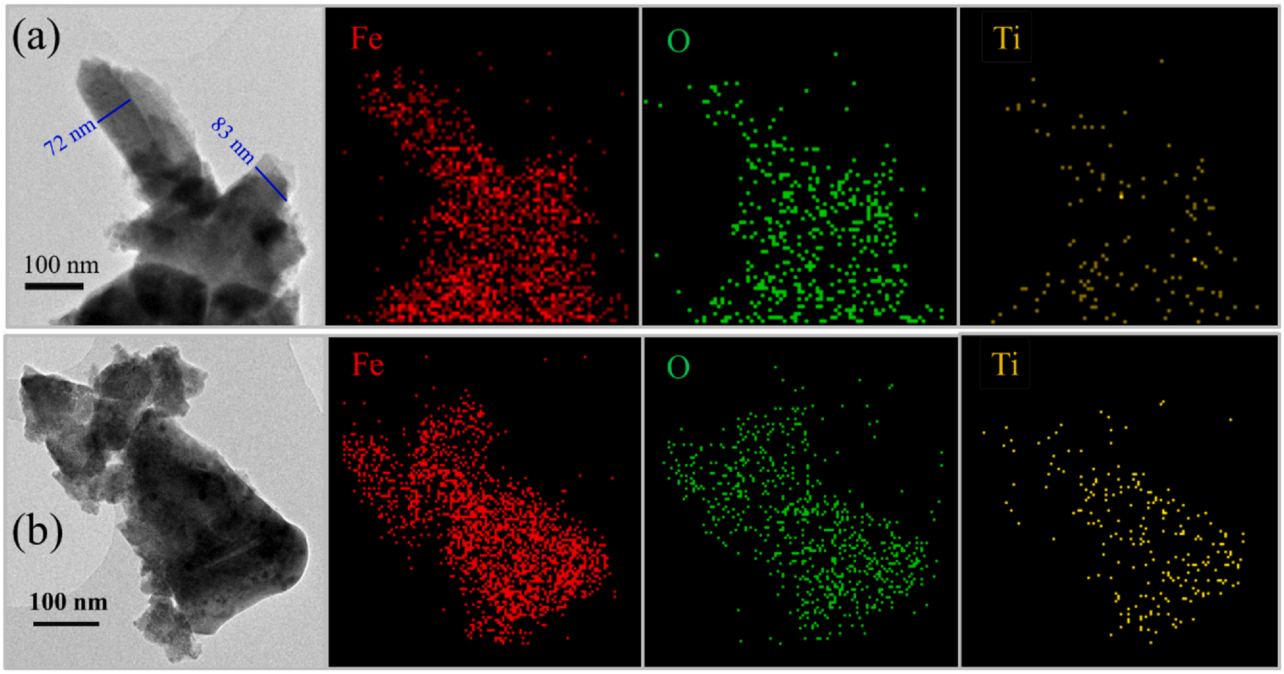

Fig. 5. TEM and corresponding TEM-mapping images of (a) Ti-4-FeOOH and (b) Ti-4-Fe_2O_3.

pristine α-Fe_2O_3, indicating that implantation-induced Ti-doping could facilitate the injection of charge carriers into electrolyte and hence enhance the performance of PEC water oxidation [29]. Among them, the optimized Ti-implanted hematite, Ti-4-Fe_2O_3, exhibits the smallest arc radius, illustrating lowest charge transfer resistance in the system. Moreover, the charge carrier densities of titanium ion implanted α-Fe_2O_3 were analyzed by Mott-Schottky (MS) measurements (Fig. 7b). The positive slopes in the MS plots reveal the n-type behavior of these photoelectrodes. The donor densities of these semiconductors have been estimated by the slopes of the MS plots (Table S3). Among all the photoanodes, Ti-4-Fe_2O_3 presents the highest charge carrier density of 7.1×10^{26} m^{-3}, which shows a 7.4-time increase in comparison to the pristine α-Fe_2O_3. The increased donor density is beneficial to the conductivity of hematite, thereby improving the collection efficiency of light-driven charge carriers [16,30].

To evaluate the effectiveness of titanium ion implantation, the photocurrent density-potential curves (i.e., LSV curves) of untreated and ion implanted α-Fe_2O_3 were conducted using a three-electrode configuration in a self-designed electrochemical system (Fig. S6). While the pristine α-Fe_2O_3 exhibits a low photocurrent density of 0.34 mA cm^{-2} at 1.23 V versus RHE under irradiation, Ti-implanted α-Fe_2O_3 with a dose of 4×10^{16} atoms cm^{-2} treatment (i.e., Ti-4-Fe_2O_3) reaches a maximum photocurrent density of 0.55 mA cm^{-2}, a ~1.6 times increase compared to pure hematite (Fig. 7c), which is consistent with the result of EIS and MS measurements. The photocurrent densities of untreated and Ti-implanted α-Fe_2O_3 with different ion doses at 1.23 V and 1.5 V versus RHE are summarized in Table S4. The dark current of Ti-dopped semiconductor was almost no change after 10 days. The degradation of PEC performance for Ti-dopped semiconductor was much slower (<5%) for the films stored under 0% RH and 50% RH after 30 days of exposure. The

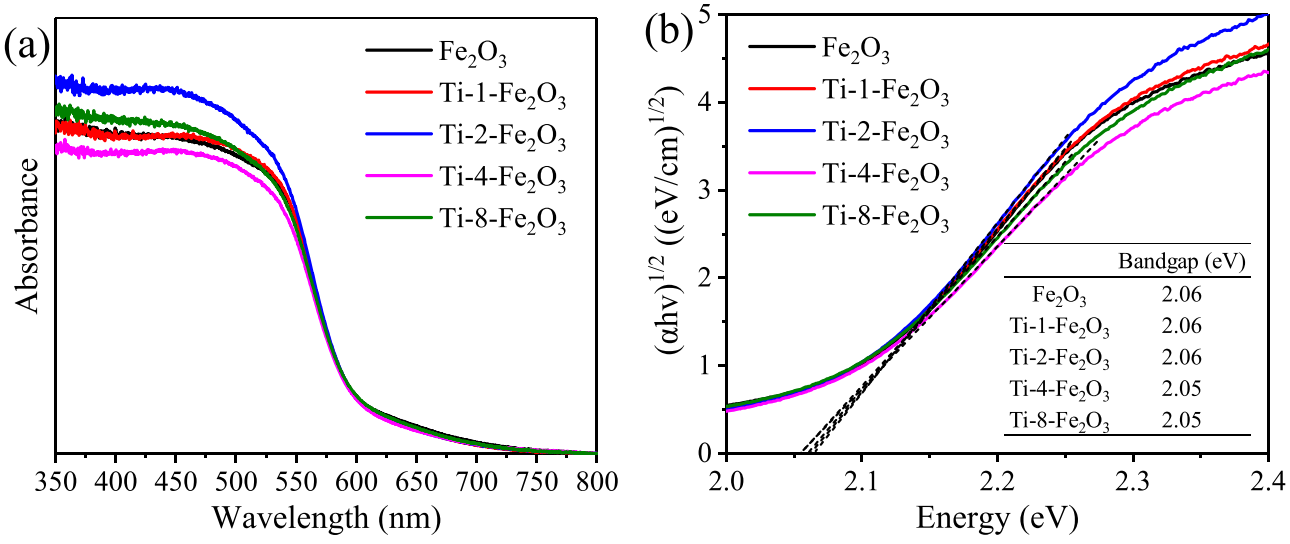

Fig. 6. (a) UV–visible absorption spectra of titanium ion implanted α-Fe_2O_3, and (b) Tauc plots of titanium ion implanted α-Fe_2O_3 for the determination of the bandgaps.

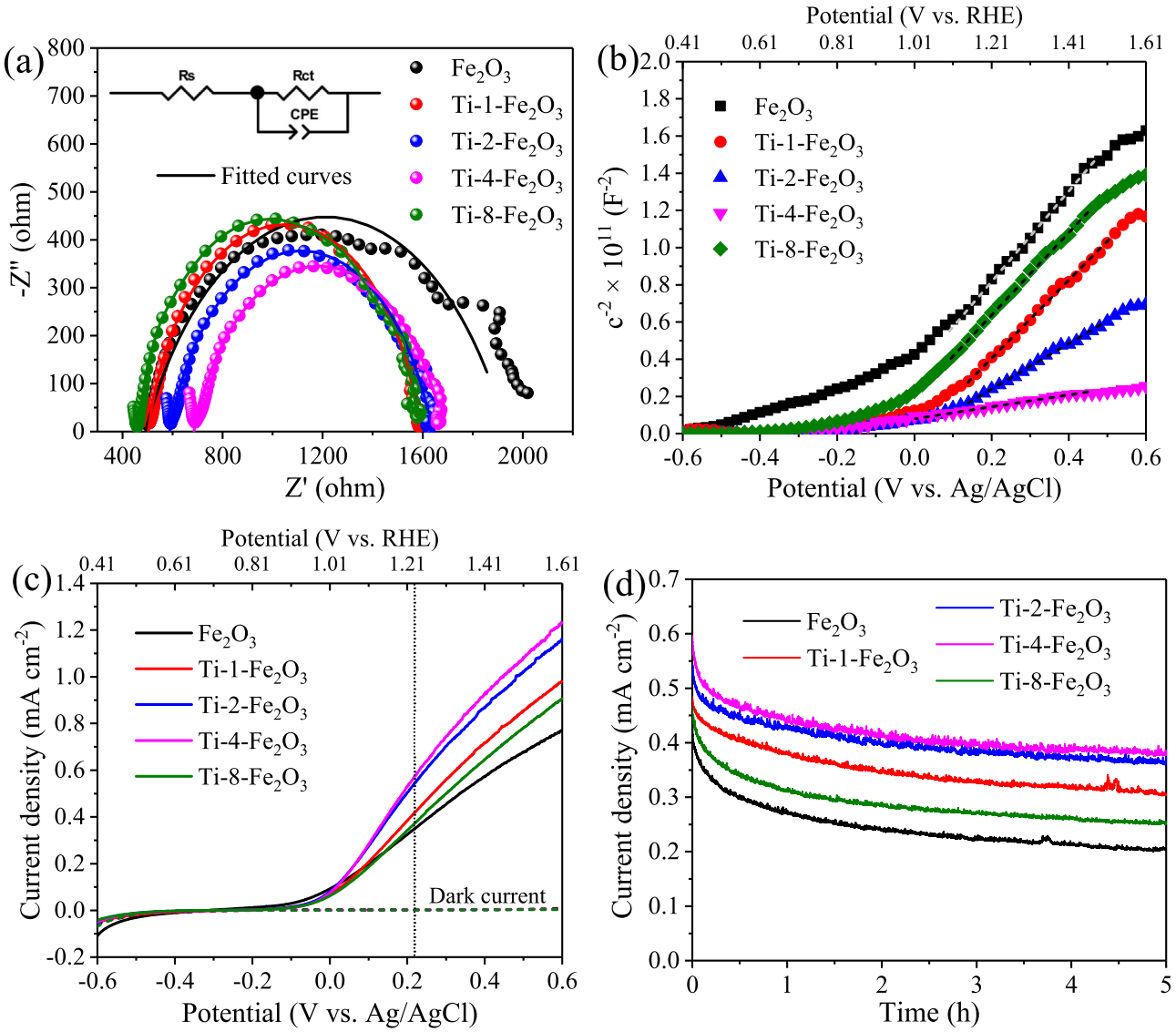

Fig. 7. Electrochemical measurements of pristine and Ti-implanted α-Fe_2O_3 at different doses: (a) electrochemical impedance spectroscopy (EIS) spectra, (b) Mott-Schottky (MS) plots, (c) linear sweep voltammetry (LSV) curves, and (d) amperometric (I-t) tests.

amperometric (I-t) measurements were performed at a bias potential of 0.22 V versus Ag/AgCl (equal to 1.23 V versus RHE) to investigate the stability of pure and Ti- implanted α-Fe_2O_3. As shown in Fig. 7d, the photocurrent of untreated α-Fe_2O_3 and as-prepared Ti plasma treated α-Fe_2O_3 gradually decreased in the 5-h measurement. Among ion implanted hematite, Ti-4-Fe_2O_3 preserves 65% of the initial photocurrent with the best current density of ~0.4 mA cm^{-2} after 5-h illumination, which is approximately twice as high as that of untreated α-Fe_2O_3.

Titanium incorporation is known to improve the PEC water oxidation performance of hematite nanostructures. Previous efforts on Ti doping strategies include hydrothermal reaction [31], solution-based deposition-annealing process [11], atomic layer deposition assisted solid-state diffusion [32], and molecular beam epitaxy growth [33]. Compared with these methods, our plasma ion implantation strategy provides the opportunity to control the amount of Ti doping in the photo-responsive materials. The PEC performance of hematite is overall determined by three processes: photon absorption, charge carrier separation and surface charge transfer. Our UV–visible absorption results together with previous works reveal that Ti doping has little influence on the bandgap of hematite [31a,34]. In addition, few studies have explored the bandgap structure changes after incorporating hematite with Ti dopants, except that density function calculation results indicate a decrease of 0.2 eV of valence band edge in Ti-doped hematite [33]. We do not observe the existence of pseudobrookite, i.e. Fe_2TiO_5, or TiO_2 in our samples, which functions to form heterojunction structure with α-Fe_2O_3, facilitating the separation of charge carriers [31,35], or passivate surface trap states and reduce surface charge recombination in hematite [36]. The main reason for the enhanced photoactivity of Ti-doped hematite could be that Ti atoms can serve as dopants and increase the major carrier density in hematite, since one vacancy is formed with the doping of three Ti (IV) atoms [33]. The hematite phase could be well-preserved without the appearance of co-existing phase, even at high Ti doping percentage (up to 17%) [33]. Besides, the high temperature treatment (800 °C for 10 min) would facilitate the diffusion of Ti atoms and further ensure a relatively uniform distribution of Ti atoms in hematite [32].

4. Conclusion

In summary, an ion implantation technique was introduced to improve the PEC water oxidation performance of hematite in this study. After the post-annealing process, titanium plasma implanted

β-FeOOH film was converted to titanium ion implanted α-Fe_2O_3 with lower charge transfer resistance and higher charge carrier density. Well-distributed Ti-doping increases charge carrier transport which simultaneously reduces the recombination of photogenerated charge carriers, therefore enhancing PEC water oxidation performance. Consequently, this work demonstrates the benefit of surface-engineered doping of hematite photoanodes using plasma ion implantation, along with a qualitative and quantitative understanding of impurity doping effects, which can provide new insights into the development of photo-responsive materials for practical applications in the emerging field of hydrogen technology.

CRediT authorship contribution statement

Y. P. and H.-Y.H. contributed to the design concept. Y. P. and Q. R. performed the fabrication process and measurements. All authors discussed the results and commented on the manuscript.

Declaration of Competing Interest

There are no conflicts to declare.

Acknowledgements

The authors acknowledge financial support from the Research Grants Council of Hong Kong (grant no. 21203518, F-CityU106/18 and 9048121), City University of Hong Kong (grant no. 7005289, 7005580, 9680208, 9667213, 9610458 and 9052029) as well as Shenzhen Science Technology and Innovation Commission (grant no. R-IND12302).

Appendix A. Supporting information

Supplementary data associated with this article can be found in the online version at doi:10.1016/j.jallcom.2021.159376.

References

[1] S. Shen, S.A. Lindley, C.L. Dong, E. Chen, Y.R. Lu, J. Zhou, Y. Hu, D.A. Wheeler, P. Guo, J.Z. Zhang, D.S. Kliger, S.S. Mao, Sol. RRL (2019) 3.

[2] D.A. Wheeler, G. Wang, Y. Ling, Y. Li, J.Z. Zhang, Nanostructured hematite: synthesis, characterization, charge carrier dynamics, and photoelectrochemical properties, Energy Environ. Sci. 5 (2012) 6682–6702.

[3] C. Miao, T. Shi, G. Xu, S. Ji, C. Ye, Photocurrent enhancement for Ti-Doped Fe2O3Thin film photoanodes by an in situ solid-state reaction method, ACS Appl. Mater. Interfaces 5 (2013) 1310–1316.

[4] (a) M. Li, Y. Yang, Y. Ling, W. Qiu, F. Wang, T. Liu, Y. Song, X. Liu, P. Fang, Y. Tong, Y. Li, Morphology and doping engineering of Sn-doped hematite nanowire photoanodes, Nano Lett. 17 (2017) 2490–2495;
(b) A.G. Hufnagel, H. Hajiyani, S. Zhang, T. Li, O. Kasian, B. Gault, B. Breitbach, T. Bein, D. Fattakhova-Rohlfing, C. Scheu, R. Pentcheva, Adv. Energy Mater. 28 (2018) 1804472.

[5] Z. Luo, C. Li, S. Liu, T. Wang, J. Gong, Gradient doping of phosphorus in Fe2O3nanoarray photoanodes for enhanced charge separation, Chem. Sci. 8 (2017) 91–100.

[6] R. Franking, L. Li, M.A. Lukowski, F. Meng, Y. Tan, R.J. Hamers, S. Jin, Facile post-growth doping of nanostructured hematite photoanodes for enhanced photoelectrochemical water oxidation, Energy Environ. Sci. 6 (2013) 500–512.

[7] (a) G. Wang, H. Zreiqat, Functional coatings or films for hard-tissue applications, Materials 3 (2010) 3994–4050;
(b) H.-Y. Hsu, L. Ji, M. Du, J. Zhao, T.Y. Edward, A.J. Bard, Optimization of lead-free organic–inorganic Tin(II) halide perovskite semiconductors by scanning electrochemical microscopy, Electrochim. Acta 220 (2016) 205–210;
(c) C. Dong, Y. Wang, H. Wang, C.S.K. Lin, H.-Y. Hsu, S.-Y. Leu, New generation urban biorefinery toward complete utilization of waste derived lignocellulosic biomass for biofuels and value-added products, Energy Procedia 158 (2019) 918–925;
(d) C.H. Mak, X. Huang, R. Liu, Y. Tang, X. Han, L. Ji, X. Zou, G. Zou, H.-Y. Hsu, Recent progress in surface modification and interfacial engineering for high-performance perovskite light-emitting diodes, Nano Energy 73 (2020) 104752;
(e) S. Rao, X. Zou, S. Wang, T. Shi, Y. Lu, L. Ji, H.-Y. Hsu, Q. Xu, X. Lu, Electrodeposition of porous Sn-Ni-Cu Alloy anode for lithium-ion batteries from nickel matte in deep eutectic solvents, J. Electrochem. Soc. 166 (2019) D427–D434;
(f) M.M.M. Bilek, A. Kondyurin, S. Dekker, B.C. Steel, R.A. Wilhelm, R. Heller, D.R. McKenzie, A.S. Weiss, M. James, W. Möller, Depth-resolved structural and compositional characterization of ion-implanted polystyrene that enables direct covalent immobilization of biomolecules, J. Phys. Chem. C 119 (2015) 16793–16803.

[8] L. Cai, F. Ren, M. Wang, G. Cai, Y. Chen, Y. Liu, S. Shen, L. Guo, V ions implanted ZnO nanorod arrays for photoelectrochemical water splitting under visible light, Int. J. Hydrog. Energy 40 (2015) 1394–1401.

[9] M. Wang, F. Ren, G. Cai, Y. Liu, S. Shen, L. Guo, Activating ZnO nanorod photoanodes in visible light by Cu ion implantation, Nano Res. 7 (2014) 353–364.

[10] L. Cai, W. Zhou, F. Ren, J. Chen, G. Cai, Y. Liu, X. Guan, S. Shen, W ion implantation boosting visible-light photoelectrochemical water splitting over ZnO nanorod arrays, J. Photon. Energy 7 (2017) 016501.

[11] (a) G. Wang, Y. Ling, D.A. Wheeler, K.E. George, K. Horsley, C. Heske, J.Z. Zhang, Y. Li, Facile synthesis of highly photoactive α-Fe2O3-based films for water oxidation, Nano Lett. 11 (2011) 3503–3509;
(b) J. Zhao, H. Yin, T. Lim, H. Xie, H.-Y. Hsu, F. Forouzan, A.J. Bard, Electrodeposition of photoactive silicon films for low-cost solar cells, J. Electrochem. Soc. 163 (2016) D506–D514;
(c) H.-Y. Hsu, H.-H. Hsieh, H.-Y. Tuan, J.-L. Hwang, Oxidized low density polyethylene: a potential cost-effective, stable, and recyclable polymeric encapsulant for photovoltaic modules, Sol. Energy Mater. Sol. Cells 94 (2010) 955–959;
(d) R. Liu, C.H. Mak, X. Han, Y. Tang, G. Jia, K.-C. Cheng, H. Qi, X. Zou, G. Zou, H.-Y. Hsu, Efficient electronic coupling and heterogeneous charge transport of zero-dimensional Cs4PbBr6perovskite emitters, J. Mater. Chem. A 8 (2020) 23803–23811;
(e) L. Vayssieres, N. Beermann, S.-E. Lindquist, A. Hagfeldt, Controlled aqueous chemical growth of oriented three-dimensional crystalline nanorod arrays: application to iron(III) oxides, Chem. Mater. 13 (2001) 233–235.

[12] C. Li, A. Li, Z. Luo, J. Zhang, X. Chang, Z. Huang, T. Wang, J. Gong, Surviving high-temperature calcination: ZrO2-induced hematite nanotubes for photoelectrochemical water oxidation, Angew. Chem. Int. Ed. 56 (2017) 4150–4155.

[13] J. Brillet, M. Grätzel, K. Sivula, Decoupling feature size and functionality in solution-processed, porous hematite electrodes for solar water splitting, Nano Lett. 10 (2010) 4155–4160.

[14] (a) S.-H. Shim, T.S. Duffy, Raman spectroscopy of Fe2O3to 62 GPa, Am. Miner. 87 (2002) 318–326;
(b) S.-S. Yi, J.-M. Yan, Q. Jiang, Carbon quantum dot sensitized integrated Fe2O3@g-C3N4core–shell nanoarray photoanode towards highly efficient water oxidation, J. Mater. Chem. A 6 (2018) 9839–9845.

[15] (a) I. Cesar, K. Sivula, A. Kay, R. Zboril, M. Grätzel, Influence of feature size, film thickness, and silicon doping on the performance of nanostructured hematite photoanodes for solar water splitting, J. Phys. Chem. C 113 (2008) 772–782;
(b) X. Zou, L. Ji, H.-Y. Hsu, K. Zheng, Z. Pang, X. Lu, Designed synthesis of SiC nanowire-derived carbon with dual-scale nanostructures for supercapacitor applications, J. Mater. Chem. A 6 (2018) 12724–12732.

[16] H. Ma, M.A. Mahadik, J.W. Park, M. Kumar, H.S. Chung, W.S. Chae, G.W. Kong, H.H. Lee, S.H. Choi, J.S. Jang, Highly self-diffused Sn doping in α-Fe2O3nanorod photoanodes initiated from β-FeOOH nanorod/FTO by hydrogen treatment for solar water oxidation, Nanoscale 10 (2018) 22560–22571.

[17] Y.Y. Fu, R.M. Wang, J. Xu, J. Chen, Y. Yan, A.V. Narlikar, H. Zhang, Synthesis of large arrays of aligned α-Fe2O3 nanowires, Chem. Phys. Lett. 379 (2003) 373–379.

[18] N. Bhandary, A.P. Singh, P.P. Ingole, S. Basu, Enhanced photoelectrochemical performance of electrodeposited hematite films decorated with nanostructured NiMnOx, RSC Adv. 6 (2016) 35239–35247.

[19] A.P. Grosvenor, B.A. Kobe, M.C. Biesinger, N.S. McIntyre, Investigation of multiplet splitting of Fe 2p XPS spectra and bonding in iron compounds, Surf. Interface Anal. 36 (2004) 1564–1574.

[20] M. Li, Y. Tang, W. Shi, F. Chen, Y. Shi, H. Gu, Design of visible-light-response core–shell Fe2O3/CuBi2O4heterojunctions with enhanced photocatalytic activity towards the degradation of tetracycline: Z-scheme photocatalytic mechanism insight, Inorg. Chem. Front. 5 (2018) 3148–3154.

[21] (a) M. Lucas, M. Yesilbas, A. Shchukarev, J.F. Boily, X-ray photoelectron spectroscopy of fast-frozen hematite colloids in aqueous solutions. 6. Sodium halide (F–, Cl–, Br–, I–) Ion binding on microparticles, Langmuir 34 (2018) 13497–13504;
(b) M.K. Islam, H. Wang, S. Rehman, C. Dong, H.-Y. Hsu, C.S.K. Lin, S.-Y. Leu, Sustainability metrics of pretreatment processes in a waste derived lignocellulosic biomass biorefinery, Bioresour. Technol. 298 (2020) 122558;
(c) J. Cao, Y. Wang, T. Ma, Y. Liu, Z. Yuan, Synthesis of porous hematite nanorods loaded with CuO nanocrystals as catalysts for CO oxidation, J. Nat. Gas. Chem. 20 (2011) 669–676.

[22] A. Wei, X. Xie, Z. Wen, H. Zheng, H. Lan, H. Shao, X. Sun, J. Zhong, S.T. Lee, Triboelectric nanogenerator driven self-powered photoelectrochemical water splitting based on hematite photoanodes, ACS Nano 12 (2018) 8625–8632.

[23] Q. Li, J. Bian, N. Zhang, D.H.L. Ng, Loading Ni(OH)2 on the Ti-doped hematite photoanode for photoelectrochemical water splitting, Electrochim. Acta 155 (2015) 383–390.

[24] D. Jaeger, J. Patscheider, A complete and self-consistent evaluation of XPS spectra of TiN, J. Electron Spectrosc. Relat. Phenom. 185 (2012) 523–534.

[25] F.L. Formal, N. Tétreault, M. Cornuz, T. Moehl, M. Grätzel, K. Sivula, Passivating surface states on water splitting hematite photoanodes with alumina overlayers, Chem. Sci. 2 (2011) 737–743.

[26] (a) S. Shen, J. Jiang, P. Guo, C.X. Kronawitter, S.S. Mao, L. Guo, Effect of Cr doping on the photoelectrochemical performance of hematite nanorod photoanodes, Nano Energy 1 (2012) 732–741;

(b) Y. Tang, C.H. Mak, R. Liu, Z. Wang, L. Ji, H. Song, C. Tan, F. Barrière, H.Y. Hsu, In situ formation of bismuth-based perovskite heterostructures for high--performance cocatalyst-free photocatalytic hydrogen evolution, Adv. Funct. Mater. 30 (2020) 2006919.

[27] (a) Y.-H. Wu, W.-R. Guo, M. Mishra, Y.-C. Huang, J.-K. Chang, T.-C. Lee, Combinatorial studies on wet-chemical synthesized Ti-doped α-Fe2O3: how does Ti4+improve photoelectrochemical activity, ACS Appl. Nano Mater. 1 (2018) 3145–3154;
(b) Z. Chen, H.-Y. Hsu, M. Arca, K.S. Schanze, Triplet energy transport in platinum-acetylide light harvesting arrays, J. Phys. Chem. B 119 (2014) 7198–7209;
(c) C.H. Mak, R. Liu, X. Han, Y. Tang, X. Zou, H.H. Shen, Y. Meng, G. Zou, H.Y. Hsu, Thermally activated delayed phosphorescence and interchromophore exciton coupling in a platinum-based organometallic emitter, Adv. Opt. Mater. 8 (2020) 2001023.

[28] J.Y. Kim, D.H. Youn, J.H. Kim, H.G. Kim, J.S. Lee, Nanostructure-preserved hematite thin film for efficient solar water splitting, ACS Appl. Mater. Interfaces 7 (2015) 14123–14129.

[29] (a) D. Ding, B. Dong, J. Liang, H. Zhou, Y. Pang, S. Ding, Solvothermal-etching process induced Ti-doped Fe2O3thin film with low turn-on voltage for water splitting, ACS Appl. Mater. Interfaces 8 (2016) 24573–24578;
(b) T.-H. Lai, I. Constantinou, C.M. Grand, E.D. Klump, S. Baek, H.-Y. Hsu, S.-W. Tsang, K.S. Schanze, J.R. Reynolds, F. So, Evidence of molecular structure dependent charge transfer between isoindigo-based polymers and fullerene, Chem. Mater. 28 (2016) 2433–2440;
(c) I. Constantinou, T.H. Lai, H.Y. Hsu, S.H. Cheung, E.D. Klump, K.S. Schanze, S.K. So, F. So, Effect of thermal annealing on charge transfer states and charge trapping in PCDTBT:PC70BM solar cells, Adv. Electron. Mater. 1 (2015) 1500167.

[30] Y. Ling, G. Wang, J. Reddy, C. Wang, J.Z. Zhang, Y. Li, The influence of oxygen content on the thermal activation of hematite nanowires, Angew. Chem. Int. Ed. 51 (2012) 4074–4079.

[31] (a) Z. Fu, T. Jiang, Z. Liu, D. Wang, L. Wang, T. Xie, Highly photoactive Ti-doped α-Fe2O3 nanorod arrays photoanode prepared by a hydrothermal method for photoelectrochemical water splitting, Electrochim. Acta 129 (2014) 358–363;
(b) P.Y. Tang, L.J. Han, F.S. Hegner, P. Paciok, M. Biset-Peiró, H.C. Du, X.K. Wei, L. Jin, H.B. Xie, Q. Shi, Boosting photoelectrochemical water oxidation of hematite in acidic electrolytes by surface state modification, Adv. Energy Mater. 9 (2019) 1901836.

[32] (a) D. Wang, H. Chen, G. Chang, X. Lin, Y. Zhang, A. Aldalbahi, C. Peng, J. Wang, C. Fan, Uniform doping of titanium in hematite nanorods for efficient photoelectrochemical water splitting, ACS Appl. Mater. Interfaces 7 (2015) 14072–14078;
(b) D. Monllor-Satoca, M. Bärtsch, C. Fàbrega, A. Genç, S. Reinhard, T. Andreu, J. Arbiol, M. Niederberger, J.R. Morante, What do you do, titanium? Insight into the role of titanium oxide as a water oxidation promoter in hematite-based photoanodes, Energy Environ. Sci. 8 (2015) 3242–3254;
(c) O. Zandi, T.W. Hamann, Enhanced water splitting efficiency through selective surface state removal, J. Phys. Chem. Lett. 5 (2014) 1522–1526.

[33] H. Magnan, D. Stanescu, M. Rioult, E. Fonda, A. Barbier, Enhanced photoanode properties of epitaxial Ti doped α-Fe2O3(0001) thin films, Appl. Phys. Lett. 101 (2012) 133908.

[34] (a) K. Maabong, A.G. Machatine, B.S. Mwankemwa, A. Braun, D.K. Bora, R. Toth, M. Diale, Nanostructured hematite thin films for photoelectrochemical water splitting, Phys. B Condens. Matter 535 (2018) 67–71;
(b) B. Klahr, S. Gimenez, F. Fabregat-Santiago, T. Hamann, J. Bisquert, Water oxidation at hematite photoelectrodes: the role of surface states, J. Am. Chem. Soc. 134 (2012) 4294–4302.

[35] (a) P. Tang, H. Xie, C. Ros, L. Han, M. Biset-Peiró, Y. He, W. Kramer, A.P. Rodríguez, E. Saucedo, J.R. Galán-Mascarós, Enhanced photoelectrochemical water splitting of hematite multilayer nanowire photoanodes by tuning the surface state via bottom-up interfacial engineering, Energy Environ. Sci. 10 (2017) 2124–2136;
(b) B. Klahr, T. Hamann, Water oxidation on hematite photoelectrodes: insight into the nature of surface states through in situ spectroelectrochemistry, J. Phys. Chem. C 118 (2014) 10393–10399.

[36] (a) F. Feng, C. Li, J. Jian, X. Qiao, H. Wang, L. Jia, Boosting hematite photoelectrochemical water splitting by decoration of TiO2 at the grain boundaries, Chem. Eng. J. 368 (2019) 959–967;
(b) X. Li, P.S. Bassi, P.P. Boix, Y. Fang, L.H. Wong, Revealing the role of TiO2surface treatment of hematite nanorods photoanodes for solar water splitting, ACS Appl. Mater. Interfaces 7 (2015) 16960–16966;
(c) O. Zandi, T.W. Hamann, Determination of photoelectrochemical water oxidation intermediates on haematite electrode surfaces using operando infrared spectroscopy, Nat. Chem. 8 (2016) 778–783.